An experimental investigation of fractal viscous fingering within and beyond the regime of low Reynolds number

PHY479
Matthew Gerry

Supervisor: Stephen Morris
Department of Physics, University of Toronto
(Dated: March 26, 2019)

We present an experimental investigation of the phenomenon of fractal viscous fingering: the interface instability associated with a bubble of a less viscous fluid displacing a more viscous fluid in a Hele-Shaw cell. We image radially expanding bubbles throughout their growth with a high-frame rate digital camera. This allows us to introduce a novel application of linear stability analysis in which the number of fingers for the fastest growing mode of the instability is computed at many points throughout the initial growth of the bubble, taking into account the variation in time of the dimensionless quantities Ca and R/b. Thus, in addition to using only initial values, we predict the number of fingers present once finite-sized fingers form by integrating the growth rates of all relevant modes throughout the linear regime. We find that, in the regimes studied, existing linear stability analyses fail to adequately predict the number of fingers that will emerge from an expanding circular bubble.

Furthermore, we use high speed image data to study the overall magnitude of the effects of shadowing and tip splitting by examining how the number of fingers on the boundary of a bubble changes throughout its growth in the nonlinear regime.

We explore these phenomena for flows described by a Reynolds number in a range between Re ≈ 0.03 (slow growth, narrow plate spacing), and Re ≈ 3.4 (fast growth, wider plate spacing).
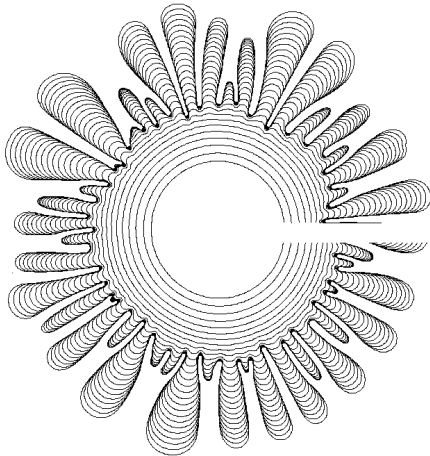
I. INTRODUCTION

FIG. 1: A composite image of the boundary of a round bubble as it grows in a Hele-Shaw cell, exhibiting viscous fingering behaviour.

A. Laplace instability in Hele-Shaw flow

Fluids often exhibit nonlinear behaviour when the solutions to the equations governing their flow are *unstable*. Here, we explore one such instability that occurs in Hele-Shaw flow, when a fluid is confined between two narrowly separated rigid plates. Hele-Shaw flow can be used as a simplifying model for the flow of viscous fluids in porous media, as occurs, for instance, in the extraction of oil from porous rock [1]. These circumstances are typically said to give rise to low-Reynolds number 'Stokes flow' [2].

Reynolds number is the familiar dimensionless parameter characterizing flow [2]:

$$\text{Re} = \frac{ub}{\nu} \tag{1}$$

where u is the characteristic speed of the flow, b the characteristic length (in Hele-Shaw flow, the spacing between the two plates), and ν the kinematic viscosity. Even at relatively high speeds, low Reynolds number can be achieved in Hele-Shaw flow due to very narrow plate spacing.

The phenomenon of *fractal viscous fingering* (or *radial viscous fingering*) occurs in Hele-Shaw flow when a less viscous fluid forms a bubble by displacing a more viscous fluid. The source of the less viscous fluid is confined to an area much smaller than the Hele-Shaw cell itself, and the apparatus is radially symmetric about the axis perpendicular to the cell at this source (taken to be the z-axis), leading to a moving fluid-fluid boundary that is initially circular [1, 3–5]. This is a variation on the problem originally explored by Saffman and Taylor, in which the fluid-fluid boundary is linear, and, spans the width of a canal, down which the boundary travels as it is pushed by the displacing fluid from the source [6].

Under these conditions, the presence of two rigid boundaries with no-slip conditions (the top and bottom
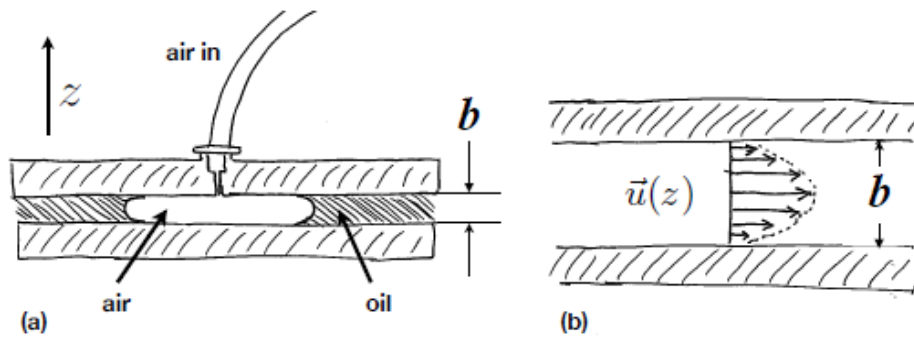
FIG. 2: (a) Air displaces oil in a Hele-Shaw cell. (b) Pressure gradients in the horizontal plane give rise to a fluid velocity with a magnitude that is parabolic in z, peaked half-way between the plates. Diagrams courtesy of Morris [5].

plates of the Hele-Shaw cell) significantly enhances the effect of viscosity, such that the viscous term of the Navier-Stokes equations of motion for fluids is said to dominate over the inertial term [2]:

$$\frac{|(\mathbf{u} \cdot \nabla)\mathbf{u}|}{|\nu \nabla^2 \mathbf{u}|} \ll 1$$

Where $\mathbf{u}$ is the velocity vector and ν the kinematic viscosity. The Navier-Stokes equations then simplify to a set of linear equations in the Stokes flow approximation [2]:

$$\nabla p = \mu \nabla^2 \mathbf{u} \qquad (2)$$

Where p is pressure and μ is molecular viscosity. The velocity of the viscous fluid varies along the z-direction, slowest at the no-slip plates and fastest exactly half-way between them [2]. However, the z-averaged velocity of the boundary can be shown to be proportional the pressure gradient:

$$\langle \mathbf{u} \rangle = -\frac{b^2}{12\mu} \nabla p \qquad (3)$$

Where b is the distance between the two plates. Since the motion of the fluid-fluid interface is precisely the motion of the more viscous fluid directly adjacent to it, and the pressure of the less viscous fluid is effectively uniform, the boundary is spatially parabolic in z and we take its velocity to be $v = \langle \mathbf{u} \rangle$ (see Figure 2) [6].

This system exhibits a Laplace instability. Since pressure obeys the Laplace equation, $\nabla^2 p = 0$, a steeper pressure gradient occurs wherever the boundary surges ahead (see Figure 3), increasing the interface velocity at that point and leading to a runaway effect wherein the boundary develops a long *finger*. This effect is limited by the constraint on the pressure drop across a curved boundary given, schematically, by [1, 5]:

$$\Delta p = \gamma \kappa \qquad (4)$$

Where γ is the surface tension, and κ is the curvature of the interface. Larger discrete pressure drops across the

boundary reduce the magnitude of the gradient in the adjacent fluids. Thus, more sharply curved interfaces, and fluids with greater surface tension, are less prone to fingering.

If, instead, a more viscous fluid displaces a less viscous fluid under otherwise identical conditions, we can see that the reverse effect occurs, creating a *stable* boundary: a point in the interface that surges ahead exhibits a lesser pressure gradient, slowing it down and allowing the rest of the boundary to catch up. Thus, this phenomenon of viscous fingering is exclusive to the case where the displacing fluid is of lesser viscosity.

B. Linear Stability Analysis

The behaviour of this boundary instability as it manifests in an expanding bubble under the aforementioned circumstances is modeled using the perturbative technique of linear stability analysis [5]. The boundary shape is said to be composed of various spatially periodic sinu-
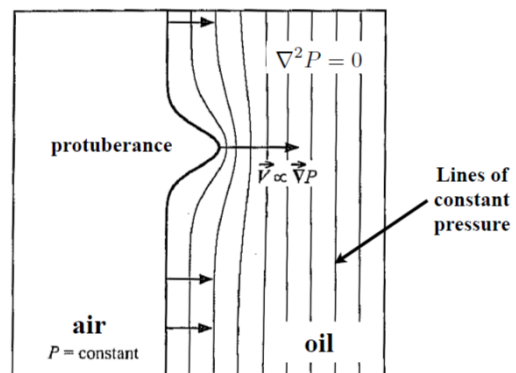

FIG. 3: The effect of a protuberance on the pressure gradient in the nearby fluid, leading to the development of a finger. Adapted from Couder [1], courtesy of Morris [5].

soidal 'modes'. In the radial situation under investigation, to satisfy periodic boundaries, each allowed mode is associated with a natural number, n, of wavelengths, corresponding to as many fingers.

While linear stability analysis is valid only in the case where the amplitude of all these modes is *infinitesimal* (i.e. in the period of the bubble's growth during which it is still round), this method predicts the number of fingers by identifying the mode with the highest growth rate during the initial growth of the bubble. That is, each mode's amplitude, ξ, changes in time with a growth rate, σ as:

$$\xi \propto e^{\sigma t} \tag{5}$$

Where $\sigma < 0$ for a stable mode, $\sigma = 0$ for a marginally stable mode, and $\sigma > 0$ for an unstable mode–the unstable modes are those growing larger, thus contributing to finger formation. The mode with the greatest value of σ at a given moment is growing the fastest–we use this to predict which mode's growth is dominant throughout the initial growth of the bubble [7]. The value of n for this mode is the predicted number of fingers. As soon as a finite-sized set of fingers forms, their own growth accelerates. Thus changes to the number of fingers may occur only due to nonlinear effects during a later phase of the bubble's growth.

Theoretical work [3, 4, 7, 8] has been done to predict at a given instant during the early life of a bubble which mode has the highest growth rate, in terms of dimensionless quantities R/b relating the radius, R, of the bubble (which is assumed to be approximately circular during the phase of initial growth) to the plate spacing, and the capillary number Ca, a dimensionless quantity relating boundary velocity to fluid viscosity and surface tension:

$$\mathrm{Ca} = \frac{\mu}{\gamma} v$$

The basis for these predictions is the determination of the specific form of the boundary condition (4) for the case of radial Hele-Shaw flow. Since there is curvature due to both the circular shape of the bubble, and the no-slip condition at the two plates, we expect a dependence of Δp on both R and b. Based on a naive prediction for Δp, the fastest-growing mode is described by [3]:

$$A_{max} = 2 \tag{6}$$

Where $A = kb/\sqrt{\mathrm{Ca}}$ is a dimensionless *modified wave number*, with $k = 2\pi/\lambda$ (the ordinary wave number). The boundary condition on Δp was derived more precisely by Park and Homsy, giving a slightly modified prediction [8]:

$$A_{max} = 2.26 \tag{7}$$

A further updated model for Δp due to takes into account the wetting layer–a thin layer of the more viscous fluid remains coating the two plates even as the less viscous fluid displaces it–and gives rise to yet another prediction for the modified wave number of the fastest growing mode, where this mode varies with varying Ca [3, 7]:

$$\frac{\pi J}{216}\mathrm{Ca}^{\frac{1}{6}} A_{max}^3 + \frac{\pi}{16} A_{max}^2 - 1 = 0 \tag{8}$$

Where in the Park-Homsy formulation, $J = 3.8$. Maxworthy [3] found (8) to agree well with experiment in the regime of very slow flows, where Ca is less than about 10^{-2}. Faster-growing bubbles were found to exhibit a smaller value of A than predicted. Note that even this most advanced prediction for the dominant mode does not account for the effects of wetting layers: the thin films of the more viscous fluid that coat the two plates, remaining in parts of the cell in which the less viscous fluid is present [5, 9].

While these predictions find the modified wave number to be a function only of Ca, the extraction of the predicted number of fingers, n, from this dimensionless quantity has further dependence on Ca, as well as on b and R. However, both Ca and R vary significantly throughout the initial (pre-fingering) growth of an individual bubble, raising the question of how to choose values of these quantities with which to calculate the predicted number of fingers. Maxworthy's predictions extract n from a single value of A, using *initial* values of R and Ca: those realized the instant bubble growth begins [3].

C. Nonlinear Features of Bubble Growth

Once finite-sized fingers have emerged in the interface of an expanding bubble, linear theory fails to predict its further behaviour as a bubble grows. However, mechanisms exist by which the number of fingers present can continue to change in this nonlinear regime.

One such mechanism is *tip splitting*. Once fingers grow large enough, their own boundaries may broaden to the point that they become subject to the same Laplace instability described in I A. Thus, while the condition of a circular expanding bubble necessary for precise linear stability analysis is no longer present, we expect to identify viscous fingering phenomena wherein a broad tip splits into two distinct fingers by a similar mechanism to that governing initial finger formation. In the regime of high Reynolds number (fast-growing bubbles), tip splitting may give rise to fractal behaviour–modeled by diffusion limited aggregation–as bubbles exhibit shapes characterized by many branching fingers [1, 5].

Conversely, *shadowing* (or *shielding*) may occur if an individual finger exhibits slower growth than the two adjacent fingers. The interface around surrounding larger moves with greater velocity, and reduces the amount of space around the smaller one occupied by the viscous fluid, limiting the magnitude of pressure gradients in that region. This slows the growth of that particular finger

(see I A). Surface tension may even cause shielded fingers to shrink, and potentially disappear [5].

II. EXPERIMENTAL SETUP AND PROCEDURE

A. Apparatus

We used a Hele-Shaw cell constructed of 2.5 cm thick acrylic plates; the bottom plate formed the floor of a 7 cm deep tank, while the top plate was a separate round piece 50 cm in diameter, with a hexagonal pattern of holes near its edge. Threaded rods through these holes with brass finger nuts fastened over top fixed the upper plate in place. Sets of six plastic spacers of a variety of thicknesses (in mm: 0.52(2), 0.791(4), 1.051(3), and 1.512(3)) set the spacing between the two plates. Spacers were either rectangular (held in place near the rods by pressure from the plates above and below) or washer-shaped (looped around the rods, in addition to being fixed by the compression from the plates). We kept the finger nuts snug, but not over-tightened, so as to prevent damage to the acrylic. We limited, to the best of our ability, spatial variation in spacing due to differences in compression between the six finger nuts. The tank was filled with heavy industrial grade mineral oil supplied by McMaster-Carr, of surface tension $\gamma = (3.3 \pm 0.1) \times 10^{-2}$ N/m, density $\rho = (0.860 \pm 0.001) \times 10^3$ kg/m^3 and molecular viscosity $\mu = 0.155 \pm 0.002$ kg/(m·s) at 22.5°C. The oil rose 3-5 mm above the bottom of the upper plate to ensure that it would fill the space between the plates (see Figure 4).

Below the tank was a large LED light, turned on during runs of the experiment, with the voltage across it held at
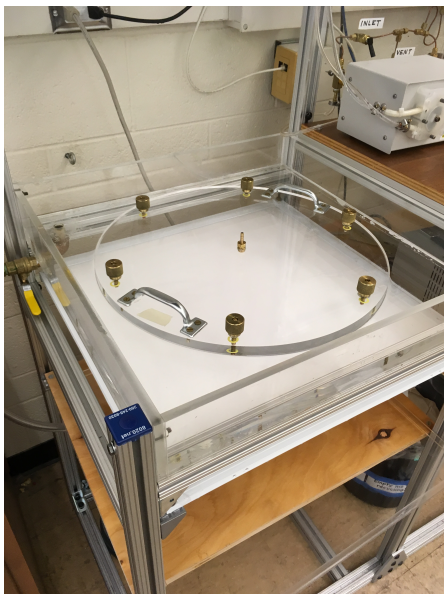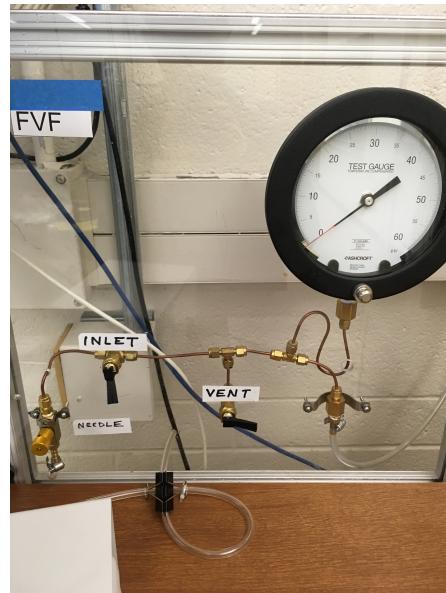

FIG. 5: The pneumatic system.

40 V by a variable a power supply. A digital camera was mounted such that its lens was about 70 cm above the tank, pointed down toward the cell; this camera was controlled through a desktop computer using `FlyCapture2` software, and took greyscale images of the Hele-Shaw cell from above. At a frame rate of 120 fps, the camera was able to capture the entire cell; in some cases, the frame rate was increased without compromising image resolution, but at the cost of capturing a smaller area.

The centre of the upper plate had an injection hole with a fixture, onto which we could attach a removable hose carrying compressed gas from a cylinder with a regulator valve. Along this hose was a large pressure gauge, a vent valve to release air from the hose without it entering the Hele-Shaw cell, an inlet valve, and a needle valve (see Figure 5). Air could only enter the cell through the injection hole when the inlet valve was held open. The speed of air entering the cell, and thus of the fluid-fluid boundary, was controlled by modulating both the pressure of the air exiting the regulator valve and the position of the needle valve.

Also attaching to the central injection hole was a removable hose connecting to a peristaltic pump, which was used to reset the apparatus before each run by drawing air out of the Hele-Shaw cell, replacing it with mineral oil that enters through the edges.

B. Procedure

1. Data Collection

Prior to a run of the experiment, a desired number of frames (TIFF images) to be captured in succession at the set frame rate was chosen in the `FlyCapture2` program.

FIG. 4: The Hele-Shaw cell.

Typically, the frame rate was set to 120 fps, though frame rates as high as 180 fps were used to capture more detail during runs of the experiment with high interface velocities.

Before each run, we pumped all air bubbles and debris that may have been present out of the Hele-Shaw cell. We set the pressure of incoming air to a desired value using the regulator valve, and when the injection hose was connected to the opening in the upper plate, we gradually let some air in, by gently opening the inlet valve, to create an initial bubble (to serve as a starting point for bubble growth). We required initial bubbles to be round; to create it, air had to be let into the cell slowly enough that the boundary instability under investigation does not take effect.

A run of the experiment consisted in clicking *start recording* on `FlyCapture2`, and subsequently fully opening the inlet valve to let air enter the Hele-Shaw cell at the rate determined by the pressure and needle valve. An air bubble would then grow in the Hele-Shaw cell. A run was complete once any air reached the edge of the Hele-Shaw cell and bubbles out (see Figure 6). Even before this point, once the fluid-fluid boundary approached closely enough to any of the six rods holding the upper plate in place, the effects of these rods on the pressure gradients in the fluid may be said to influence the boundary shape, rendering the run effectively over. After each run, we deleted images (frames) captured before bubble growth began and after the run ended.

Once every 4-6 runs, we removed the top plate and rotated it (some multiple of 30 degrees, as permitted by the hexagonal geometry of the fixtures), to reduce the influence of small imperfections in the rotational symmetry of the apparatus on finger growth in any particular direction. We used a single piece of masking tape on the edge of the upper plate to keep track of its angular position. We typically conducted 5-10 runs of the experiment at the same adjustable parameters (pressure, needle valve setting, and plate spacing).

2. Data Processing

Images were processed using `ImageJ` and Python Image Library (PIL). A centre pixel could be identified in `ImageJ`. Then, for each image, a PIL image matrix was created and a minimum and maximum radius was set so that pixels in the centre (around the injection hole) and near the edge (finger nuts) could be removed. Pixels were also removed along a horizontal band of a set thickness (usually about 50 pixels) from the centre to the right side of each image, to remove the injection pipe. In what remains after these modifications, the darkest pixels in the image are those depicting the fluid-fluid boundary. Thus, threshold values (typically between 90 and 140, on a scale from 0–black–to 255–white) could be set such that only the boundary is darker than the threshold; binarized images were produced in which the interface is a black
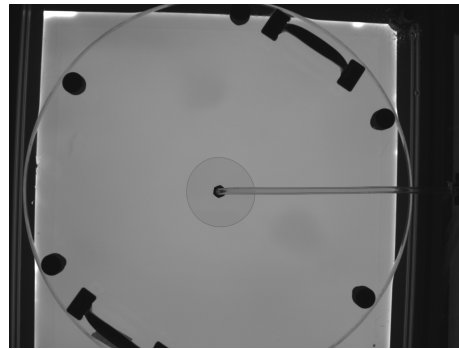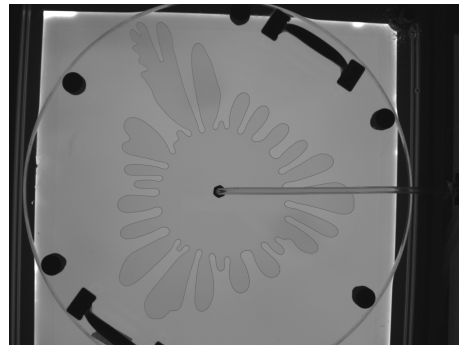

(a) A run begins with an initial bubble.
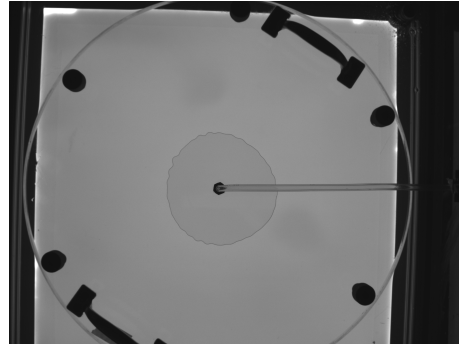
(b) Finite-sized fingers begin to form in the boundary.
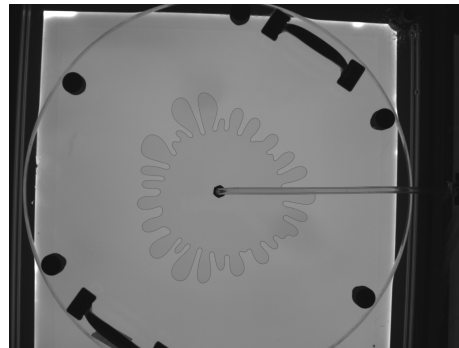
(c) Fingers increase in size as bubble growth progresses.

(d) The run ends as the boundary reaches the edge of the Hele-Shaw cell

FIG. 6: Unprocessed images of a bubble's growth captured throughout one run of the experiment (3 psi, 0.52 mm plate spacing).

curve on a white background, by turning all pixels darker than the threshold black, and all others white (see figure 7). Usually, we created a binarized image of every photograph taken in a run. Sometimes, when there were many frames recorded (slower flows, 500-2000 frames), the data was decimated, and only one in every set of some number of frames (values between 2 and 10 were used) was binarized and used for analysis.
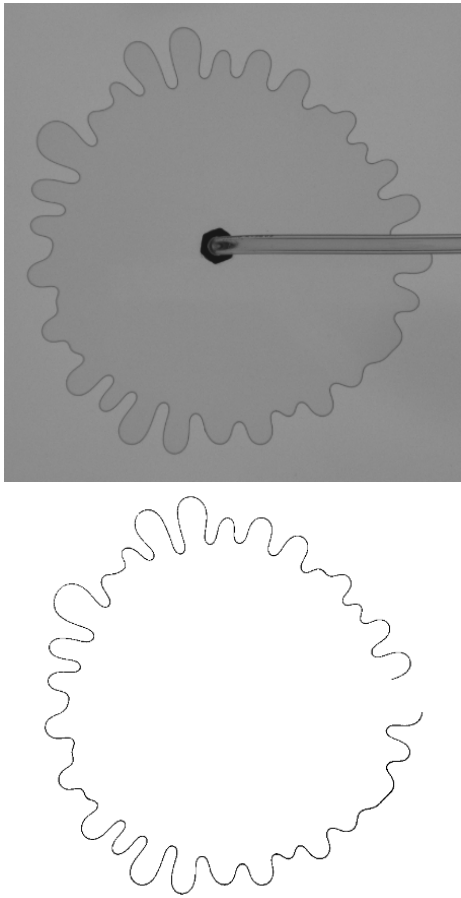

FIG. 7: A greyscale image captured during a run of the experiment and its processed, binarized counterpart.

Desired information–namely, interface radius and velocity, as well as standard deviation in the radius, which would grow as nonlinear effects take over–could be extracted from the set of binarized images produced of each run of the experiment. This was also done in Python, by using the position of each black pixel in the binarized images to compute its radial (r) and angular (ϕ) coordinates. A pixel corresponding to the centre of the bubble was chosen for each run by fitting a plot of r vs ϕ for the first frame to a cosine curve of period 2π, and using the choice of centre-pixel that returned the smallest amplitude. Then, the average radial coordinate of all black pixels in each image from the run was computed to describe how the average radius changes through the run. In the linear regime, the average radius is approxi-

mately the radius of the bubble. Polynomial fitting (3-5 degrees of freedom) was then used to describe radius as a function of time (frame number divided by frame rate); this polynomial was differentiated to describe the interface velocity throughout the run. These velocity values could then be multiplied by the necessary factors to obtain capillary number and/or Reynolds number values. This radius and velocity data was used to perform linear stability analysis on the data, for predictions regarding the number of fingers that would form in each run (see III A).

We counted the number of fingers (n) that formed in each run (to compare to the predictions of linear stability analysis) manually, by selecting a frame from shortly after the fingers corresponding to the dominant mode grew to finite size. In some cases, we also investigated how the number of fingers changes *throughout* a run. To achieve this, in addition to manually counting fingers, we employed a Python program that automatically counted the number of fingers present in every frame of a run (see Appendix A).

Appendix B lists the names and purposes of all of the Python scripts we used to process and analyze the data.

C. Experimental Limitations

1. Limits on Reynolds Number

The low end of the range of Reynolds number values we were able to explore was determined by the capabilities of the apparatus itself. The slowest flow achieved was with the narrowest spacers (0.52 mm) in, the pressure at 2 psi, and the needle valve just under one half-turn open (out of a total of three full turns). These runs exhibited capillary numbers in a range between 0.03 and 0.1 (see Figure 8a), where the highest value obtains at the start of bubble growth, and the boundary speed slows as the bubble grows larger and the air pressure is spread over a larger fluid-fluid interface. This corresponds to a Reynolds number range between 0.015 and 0.06 (order 10^{-2}), with an average Reynolds number throughout the linear regime of about 0.03. For bubble growth any slower than this, the interface would stop moving part way through a run, when the bubble reached a critical size at which the incoming air pressure was not enough to overcome opposing pressures and surface tension.

The upper end of the Reynolds number range explored was determined by our capacity to collect meaningful data in the linear regime (before finger formation). With a functional upper bound on our camera of 180 fps, bubbles growing too quickly would form fingers before enough frames could be collected to adequately use a polynomial fit to measure the speed of their growth while they were still circular. Since we require this speed data to run our linear stability analysis, we were limited to bubbles growing slowly enough to collect about ten or more frames in the linear regime. The fastest flows we
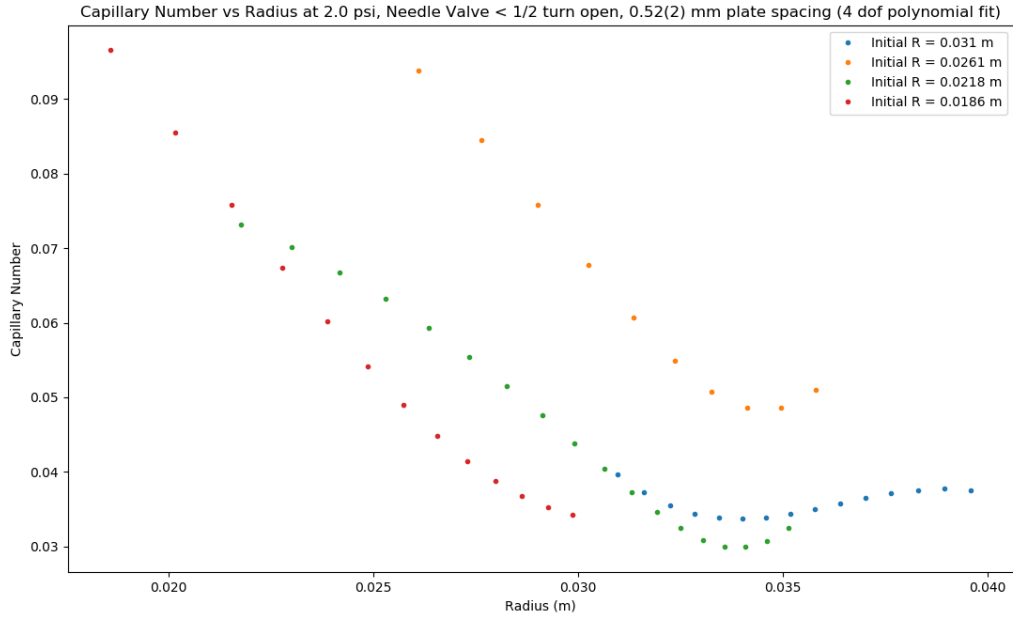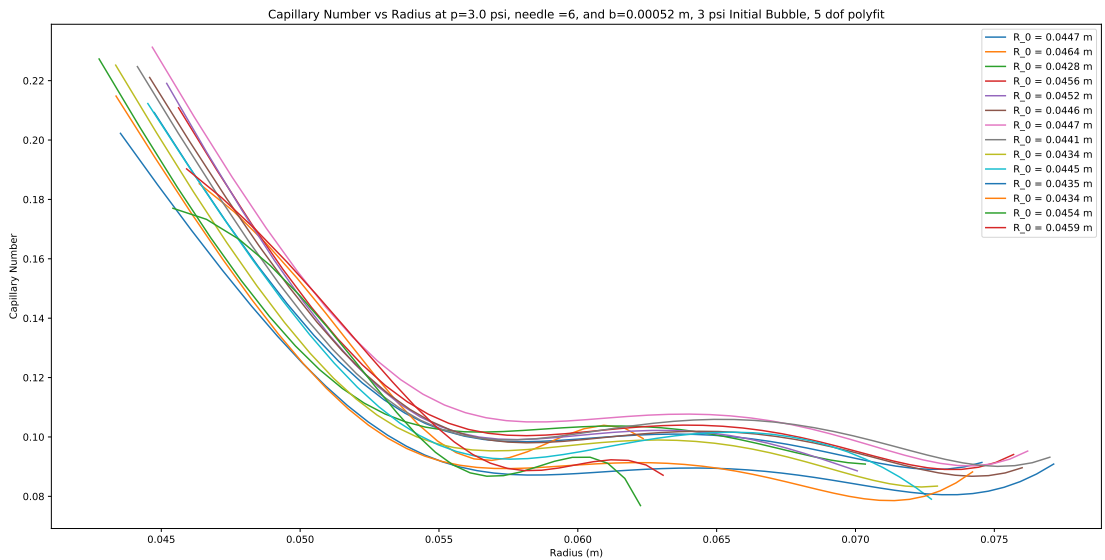
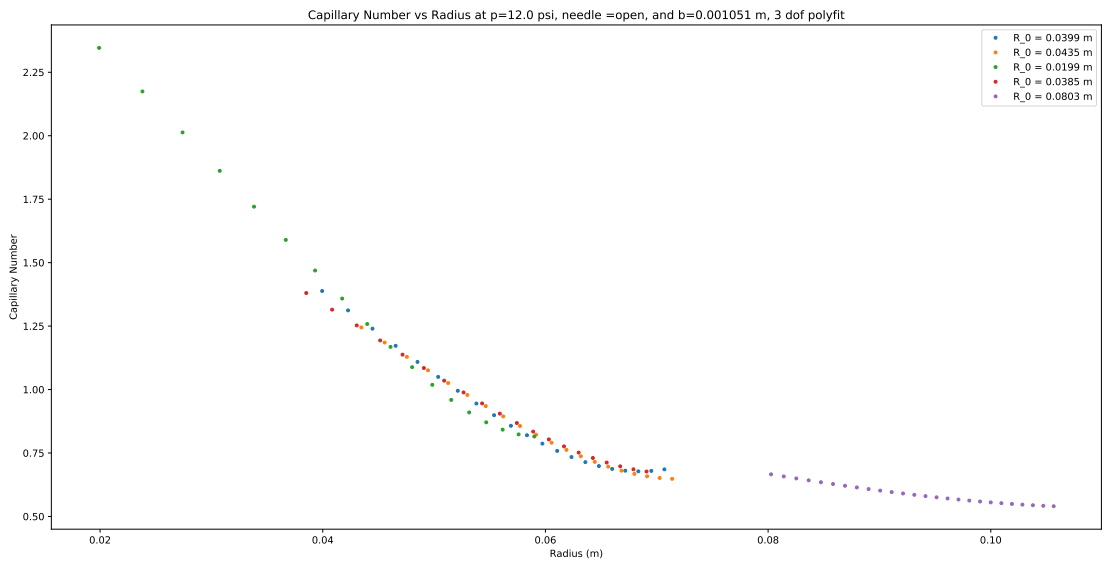(a) The slowest flows studied: 2 psi with 0.52 mm plate spacing.
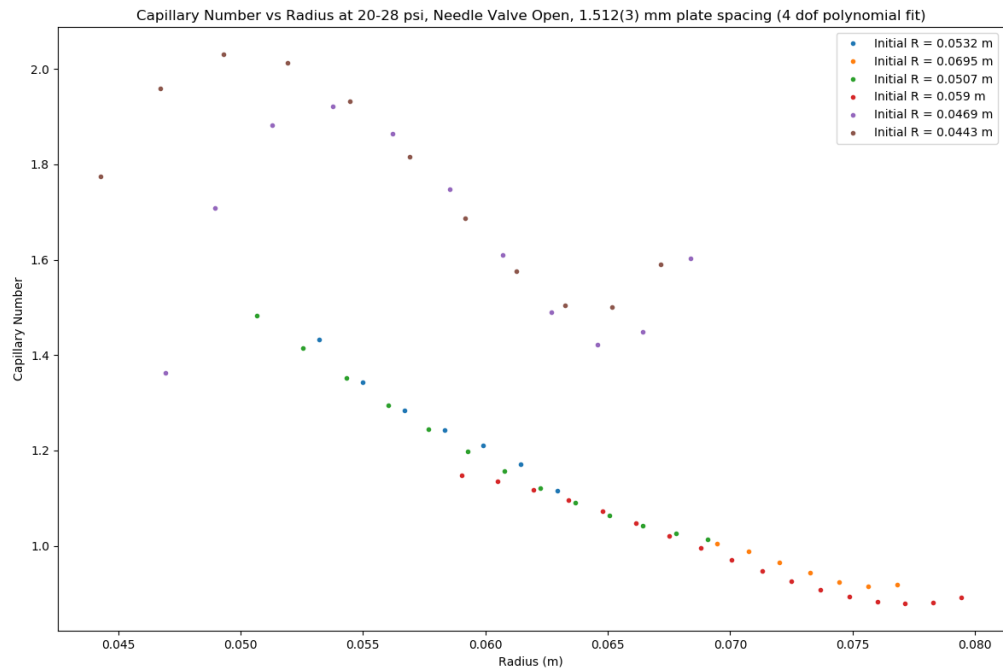
(b) The fastest flows studied: 20-28 psi with 1.512 mm plate spacing.

FIG. 8: Capillary number vs. radius throughout the linear regime for the slowest and fastest flows examined.

(a) Runs at 3 psi with 4.5 cm initial bubble radius and 0.52 mm plate spacing.

(b) Runs at 12 psi with varying initial bubble radii and 1.051 mm plate spacing.

FIG. 9: Capillary number vs. radius throughout the linear regime exhibited consistent behaviour, even as the initial radius of the run varied.

were able to study occurred with the thickest spacers (1.5 mm), and the pressure set between 20 and 28 psi, with the needle valve wide open. Under these conditions, capillary number ranged between 0.8 and 2.1 and Reynolds number between 1.5 and 3.4, averaging around 2.2 (see Figure 8b).

Our apparatus could be used to study fractal viscous fingering phenomena at pressures (hence, speeds) far higher–up to about 50 psi–if sufficient data in the linear regime for stability analysis is not required. For instance, future experiments may involve running at these higher pressures to collect data for the study of fractal branching behaviour in the nonlinear regime.

2. Stochastic Elements and Consistency

While the Laplace instability responsible for fractal viscous fingering is a well-understood result of fluid mechanics, the onset of finger formation during any given run is due to inherently stochastic processes. In an idealized version of the experiment, the Hele-Shaw cell is perfectly rotationally symmetric about the perpendicular axis through the injection hole, and the unstable dynamical equilibrium of the circular boundary is broken by an assumed uniform perturbation, allowing all modes of the instability to grow during the linear regime at rates predicted by linear stability theory (see I B). In reality (or anything remotely close), despite attempts to control for imperfections, such as rotating the upper plate and ensuring near equal torque on all six finger nuts, small deviations from this rotational symmetry (imperfections in the surface of the plates, spatial variations in the plate spacing, etc.) allowed protuberances like those discussed in I A to form, initiating finger formation. In addition, these imperfections would often cause the initial bubble of a run to become elliptical in shape, or off-centre, before the run began. The overall result was, in many cases, that fingers would begin to form in one region of the boundary before forming elsewhere (see Figure 10). We often found this effect to propagate throughout the entire run, with the fingers that formed first reaching the edge of the cell first. Rotating the upper plate (holding all other parameters equal) was found to cause the region of earliest finger formation to move to a different part of the interface.

Despite this, runs at the same settings for all adjustable parameters (spacing, pressure, needle valve, size of initial bubble) consistently resulted in similar finger counts. This was most extensively tested with the 0.52 mm spacers, at 3 psi, with the needle valve just over one half turn open, and the initial bubble radius 4.5(2) cm. We achieved consistency in initial bubble radii by setting the regulator valve to 3 psi, closing the auxiliary valve on the gas cylinder, and slowly emptying the injection pipe into the cell. We then re-opened to the auxiliary valve for the run. In doing this, care must be taken to begin the run shortly after the initial bubble is produced, before
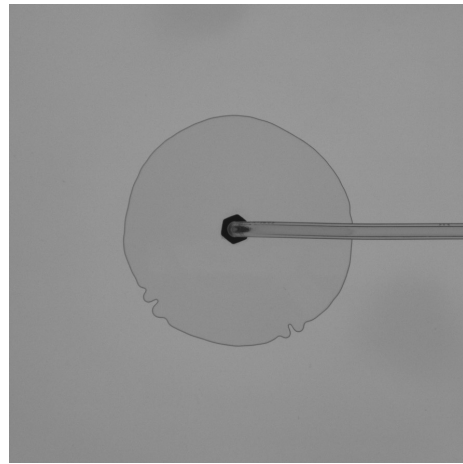

FIG. 10: Finger formation begins in some regions of the boundary before others.

the oil from the wetting layer on the upper plate forms droplets; this is easier with more narrowly spaced plates, when the lower Reynolds number manifests in longer time scales for flow.

We conducted fourteen runs at these parameters, periodically rotating the plate, for an average of 28.5 fingers with a standard deviation of 3.0 fingers. This gives a random error of 0.9 fingers: significantly less than the 'counting uncertainty', which ranged between 2 and 5 for each run, and is due to slight ambiguity concerning which boundary curvature elements we identify as fingers when counting.

Furthermore, we found that holding the adjustable parameters constant led to good consistency in interface velocity between different runs. See Figure 9a–despite some variation in the length of the runs, the capillary number as a function of radius throughout each run, as determined by Numpy polynomial fits, exhibit very similar curves. The continuity equation for fluid mechanics would suggest that these curves decay as R^{-1} to leading order.

We also found this consistency in boundary velocity to generalize when we varied the initial radius (See Figure 9b). This observation may support the claim that the Stokes Flow approximation applies in this situation: a negligible inertial term in the Navier-Stokes equations manifests in the boundary speed depending only on its radius, and the pressure of the air driving it, and not on whether it is *already in motion.*

III. FINDINGS

A. Results of Linear Stability Analysis

We applied the linear stability analysis methods discussed in I B (equation (8)) in two ways: (1) assuming that the parameters Ca and R identified at the start of
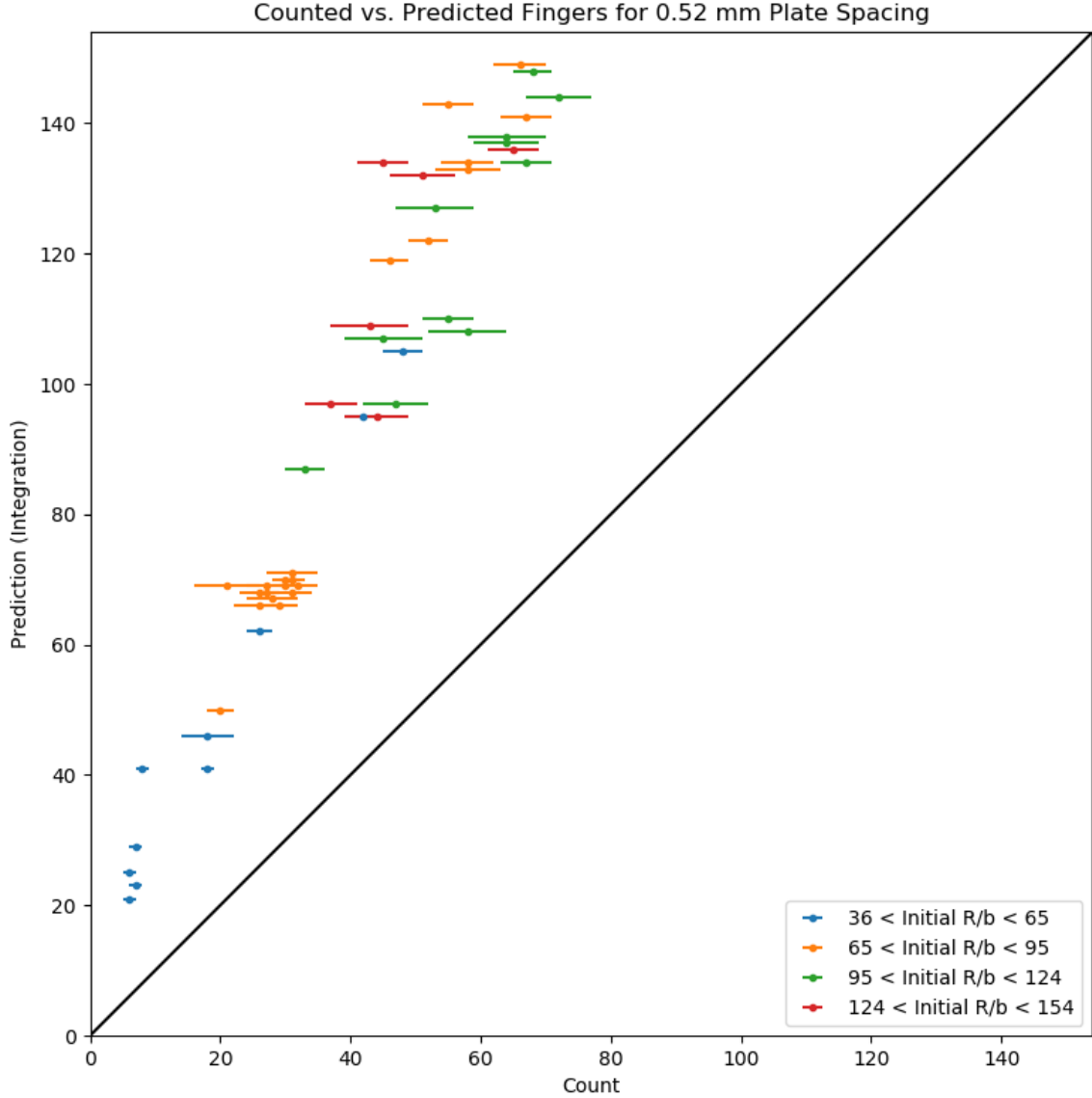
FIG. 11: Predictions of linear stability analysis against counted values of n for 0.52 mm plate spacing.

the run are sufficient to predict the mode of the instability with the maximum growth, matching the method of Maxworthy [3], and (2) using Python to compute the growth rates throughout the linear regime (examining all frames before the formation of finite-sized fingers), and integrating throughout this phase of each run to identify a mode with the maximum overall growth. 'Instantaneous' values of all variables required could be obtained from the polynomial fits for R and v at each frame in a given run (from which the dimensionless variables of

interest, R/b and Ca, are calculated); a numerical integration computed growth rate of the various modes, up to a maximum number of 200 fingers (well above any value of n predicted or observed) and identified the one with the greatest global growth.

In general, both applications of linear stability analysis failed in the regimes studied even to serve as reasonable leading-order approximations, predicting values for n as high as double those observed. Figures 11, 12, 13, and 14 plot the number of fingers predicted by linear
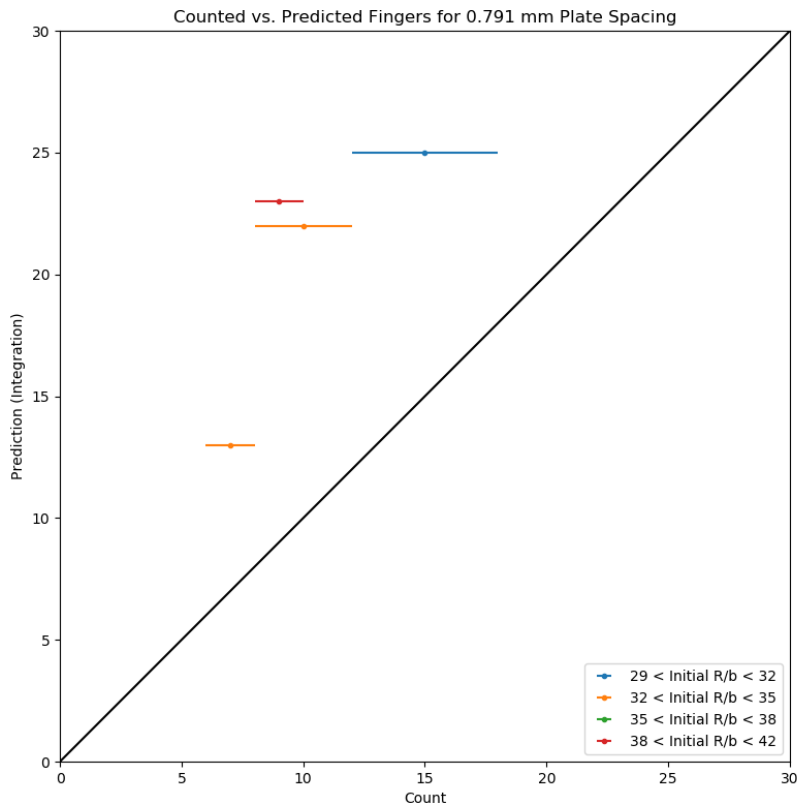
FIG. 12: Predictions of linear stability analysis against counted values of n for 0.791 mm plate spacing.

stability theory on the vertical axis, against the counted numbers of fingers for corresponding runs; the positioning above the diagonal of virtually all points indicates that linear stability theory consistently predicted values of n higher than what we observed. Our plots separate runs into coarse-grained categories based on initial bubble sizes. As expected, larger initial bubbles gave rise to larger predicted and counted values of n. Maxworthy [3] found good agreement between theory and experiment for flows slower than the ones we studied here ($\log_{10} \mathrm{Ca} \leq 2$), but showed results deviating from theory for faster flows (in the lower end of the regimes we studied). Our experiment raised the upper bound of interface speeds examined into the regime where $\log_{10} \mathrm{Ca} \approx 0.3$. No existing experimental findings suggest that linear stability analysis adequately predicts the dominant mode for viscous fingering in these regimes. Indeed, for flows with higher Reynolds number (characterized by higher speed and length scales), we should expect the Stokes flow approximation, wherein the inertial term in the Navier-Stokes equations is said to be negligible, not to apply. Since it is this very approximation from which the predictions for the growth rates of the various modes are de-

rived, the failure of linear stability analysis in this regime is not taken as a surprise.

We saw the best agreement between theory and experiment for runs conducted with the greatest plate spacing (1.512(3) mm). In these runs, at lower speeds, the two predicted values of n were typically within five fingers of the observed value (See Figure 15b), and the discrepancy between linear stability theory and experiment grows gradually with capillary number (and thus, at fixed spacing, Reynolds number), as we may predict given the decreasing validity of the Stokes flow approximation. The widest plate spacing corresponds to the regime of highest Reynolds number (0.2 to 3.4), where we expect our theory to fail due to the failure of the Stokes flow approximation. However, wider plate spacing also corresponds to the situation where the wetting layers on the plates make up the smallest proportion of the distance between them (assuming the thickness of these layers varies relatively little with plate spacing itself). Since our theoretical model does not account for these wetting layers, improved correspondence to experiment in cases where the wetting layers are the least significant suggests that the failure of the theory may be attributed in part to the role
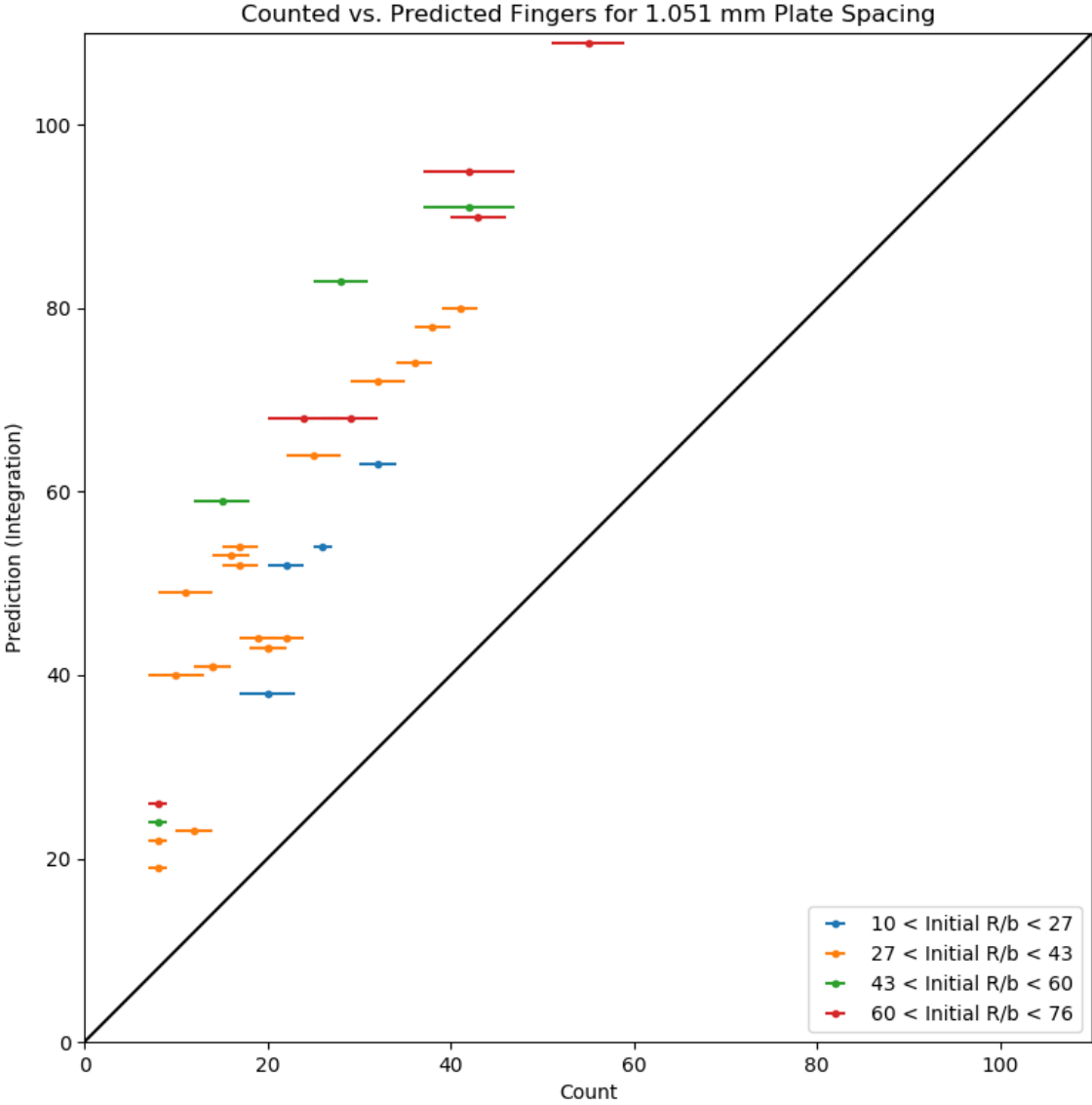
FIG. 13: Predictions of linear stability analysis against counted values of n for 1.051 mm plate spacing.

played by these layers in the fingering phenomenon. The larger gap between theory and experiment with lesser plate spacing is then explained by the fact that wetting layers in these cases, occupying a larger proportion of the vertical distance between the two plates, may be more relevant to determining the value of n realized.

For most runs, the linear stability analysis method making use of integration over growth rates throughout the linear regime returned predictions for n slightly greater than that making use only of initial growth rates

(see Figure 15). We attribute this to the fact that the integration method accounts for predicted finger growth as the bubble's radius, R increases, and not only at its initial (and smallest) value of R. An increase in R theoretically gives rise to two opposing effects. Firstly, with the incoming air at fixed pressure, a larger radius, and hence, a larger fluid-fluid interface, means a slower interface velocity, and thus a lower value of the modified wave number, A, for the mode with the greatest instantaneous growth rate (see I B). However, with a larger radius, a
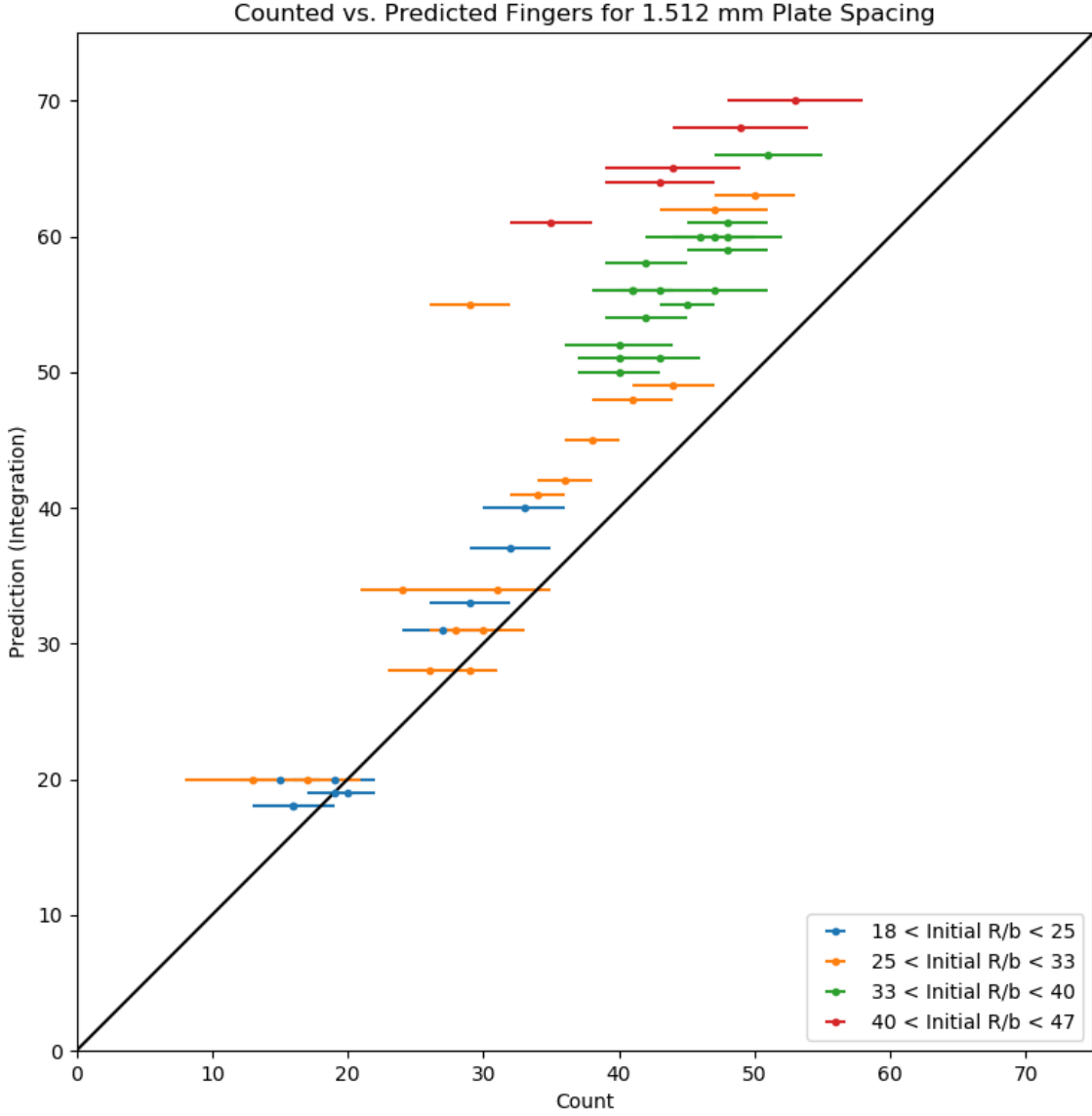
FIG. 14: Predictions of linear stability analysis against counted values of n for 1.512 mm plate spacing. Here, the proximity of points to the diagonal, particularly for runs with fewer than 30 fingers, demonstrates the greatest success we found for the predictions of linear stability analysis.

greater number of wavelengths for a given modified wave number fit along the boundary, leading to a larger predicted value of n. We see that this latter effect is more significant; even though the additional data taken into account by the integration method corresponds to slower growth, the increased size of the boundary as the bubble grows leads the model to predict more, not fewer, fingers.

This resulted in the integration method giving predic-

tions for n that deviate further than the initial value-method's predictions from experimental values. However, the difference between these two predictions was typically significantly less than their deviation from the observed value of n. Therefore, we do not conclude that the model in which only initial values of R/b and Ca affect bubble growth is more accurate than the one in which values of these quantities throughout the entire period of
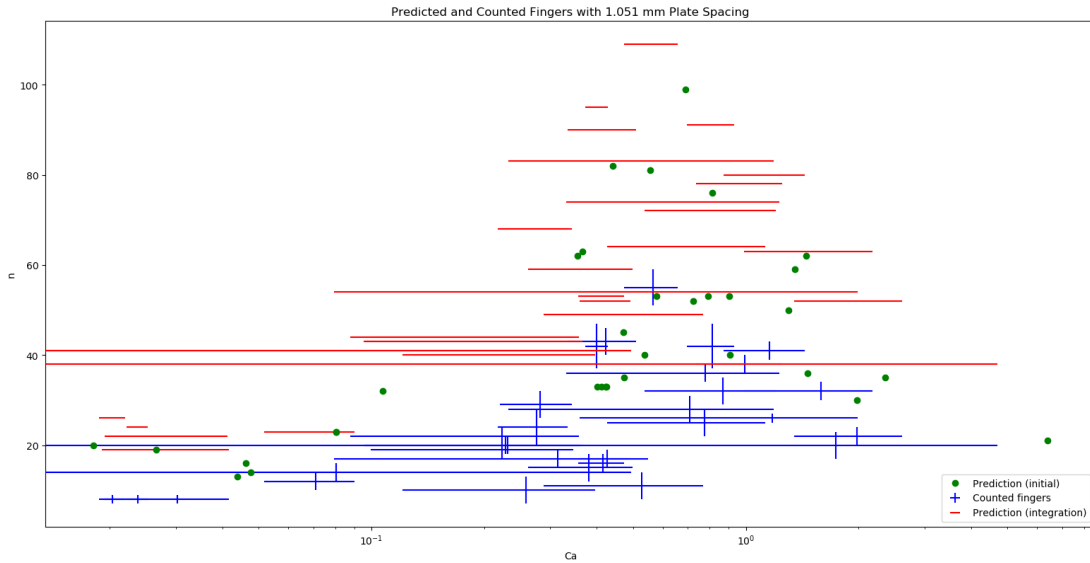
(a) Predictions and counts for n with 1.051 mm spacing.
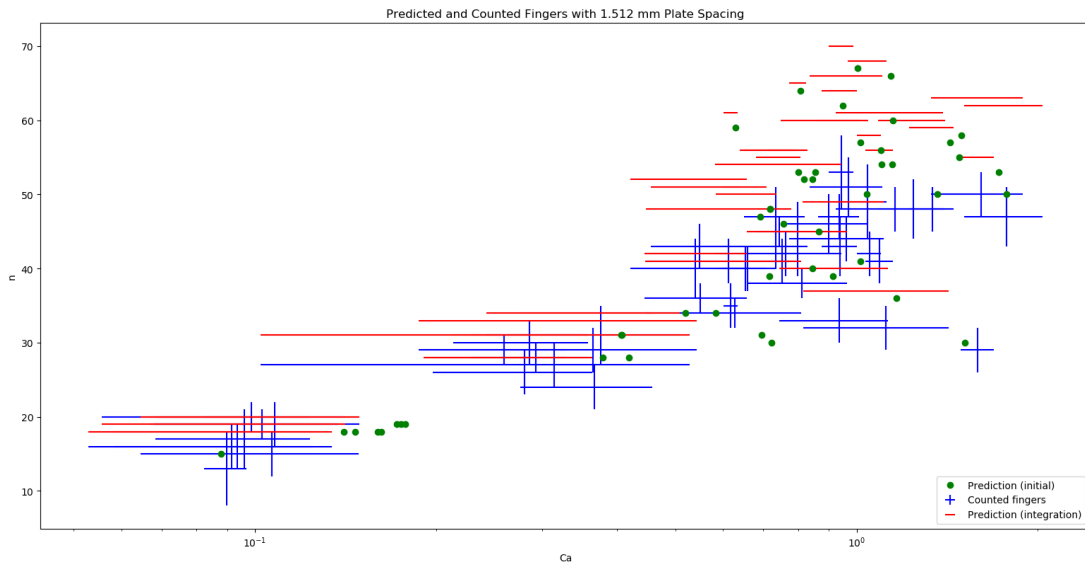
(b) Predictions and counts for n with 1.512 mm spacing. The runs at lower capillary number for this plate spacing exhibited the closest correspondence between theory and experiment.

FIG. 15: Both integration and initial-value predictions, as well as manual counts. The horizontal bars span the range of capillary number values obtained throughout each run. The points correspond to the initial-value predictions, and are located at the value of Ca associated with the beginning of each run. The integration method typically predicted a slightly higher value of n than the initial-values method.

initial growth (prior to fingering) are taken into account. In fact, the Stokes flow approximation effectively states that the 'history' of a fluid flow does not affect its behaviour. Thus, if the bubble remains qualitatively round for a finite period of time at the start of its growth, we are not in a position to conclude that any special role is played by its radius and interface velocity at the instant its growth begins. Therefore, in any situation for which our models more accurately predict n values, we should expect the integration method to perform better than the initial values-method.

Furthermore, future investigations may involve a novel method: one which makes predictions for the dominant mode by taking into account *only* values for R/b and Ca for a small time interval around the end of the linear regime, when finger formation occurs. This model could be made more advanced by taking into account the fact that finger growth begins at different times in different regions of the boundary II C 2. Therefore, the prediction for n would be computed from a combination of different dominant modes corresponding to different regions of the boundary, each determined by the values of R/b and Ca that obtained when finger growth began in its respective region.

However, the failure of linear stability analysis to predict the results of our experiment is primarily taken as a more general indication of the discrepancy between the instability giving rise to finger formation in reality, and the type of instability the theory implicitly assumes to be at play. The theory is based on a sort of *white noise* perturbation that places all modes on an equal footing, allowing their growth rates to be computed by the methods discussed in I B. On this assumption, each mode is effectively growing with infinitesimal amplitude throughout the linear regime, and integrating growth rates as we have done provides the most mathematically legitimate description of how the interface instability is believed to behave. In the experiment, stochastic systematic features (uneven plate spacing, imperfections in the plate materials, elliptical nature of initial bubble, etc.–see II C 2) play a role in initiating finger growth that we believe to be the dominant factors affecting mode selection. The linear theory cannot account for the way that these factors may favour certain modes, and influence where and when finger formation begins. Thus, future investigations should attempt to minimize these systematic flaws, for instance by constructing Hele-Shaw cells with smoother and more rigid materials, and using a method for setting the plate spacing that applies pressure more evenly around the perimeter of the cell.

### B. Shadowing and tip splitting in the Nonlinear Regime

We qualitatively investigated the effects of shadowing and tip splitting (see I C) on the realized value of n by using our finger counting algorithm to count the number of fingers present in every frame collected during a few selected runs. This algorithm was found to be accurate to within about 3 fingers for our runs with the greatest values of n; most error was due to the gap in our binarized images where the inlet pipe was removed. We plotted n against t for individual runs. In general, we found that for the Reynolds number ranges under investigation, after the phase of initial finger growth, each bubble would settle on a value of n, at which it would remain for a significant portion of the run (see Figure 16a). This value was typically the one associated with the dominant mode in the linear regime. In some cases, this value of n would be the final one; tip splitting and shadowing would not have a significant effect on the overall number of fingers present. For faster flows, the tip splitting instability would sometimes cause n to begin to increase late in the run, as the tips of the fingers began to broaden enough that smaller pressure drops across the boundary, as given by equation (4), allowed for large enough pressure gradients in the fluid for the Laplace instability to generate a finger. Figure 17a represents the boundary at the end of a run where the pressure was set to 5 psi with 1.051 mm spacing; blue dotted lines track where finger tips have been present throughout growth.

One exception to this was bubbles with relatively few fingers overall. We tracked n throughout a run for which only 7 fingers were observed to emerge in the linear regime (see Figure 16b). In this case, each finger occupied a relatively large angular region of the boundary, and so had a chance to broaden to the point that tip splitting could occur, even with the lower interface speed (see Figure 17b). Here, n steadily and gradually increased throughout the run.

Shadowing did occur on the boundaries of the bubbles studied–many fingers were stunted in their growth by larger surrounding fingers–but pressure gradients and surface tension did not typically cause more than one or two shadowed fingers for any given bubble to *fully disappear*. When this did happen, it did so relatively early in a run. Blue dotted lines in Figure 17 that do not terminate in a red 'X' indicate the few cases where shadowing led to the complete disappearance of a finger. Usually, shadowing would cause fingers to remain small, but present.

For the regimes studied, (Re ≈ 0.03 to Re ≈ 3.4), we conclude that the effects of tip splitting and shadowing were present, but rather limited. When they did affect the number of fingers present throughout a run, they never led to ambiguity in how many fingers were associated with the dominant mode in the linear regime. We would expect the tip splitting instability to have a more significant effect for faster-growing bubbles, where steeper pressure gradients around the interface would mean less broadening of the tips is required for them to split.
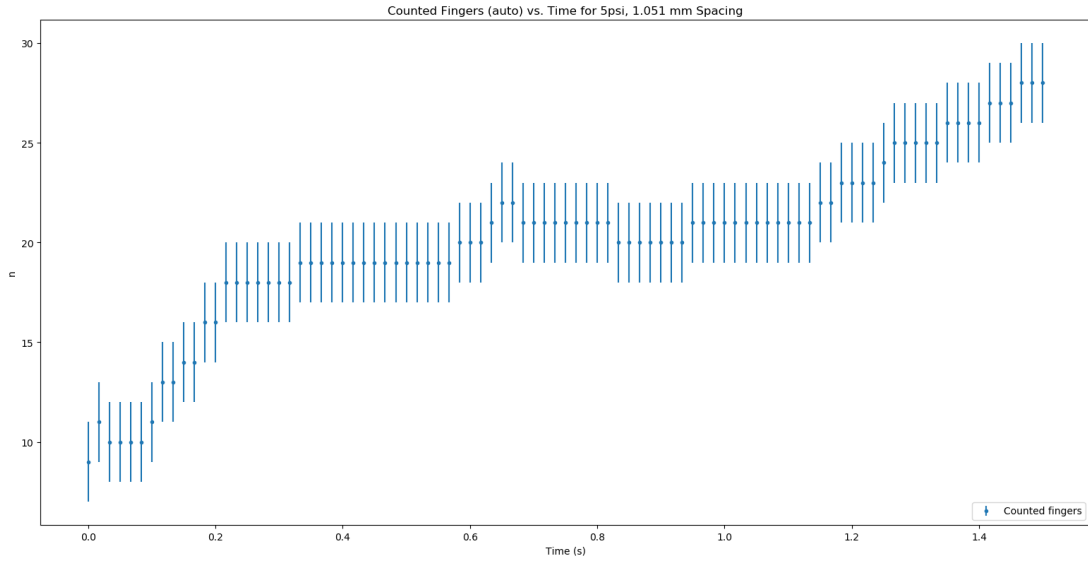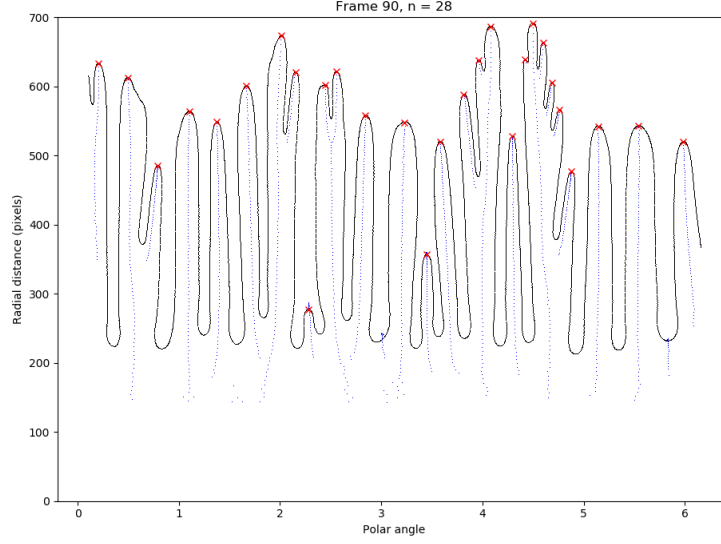
(a) n reaches a value after the linear regime, where it remains for a period of time and then begins to grow again toward the end of a run.
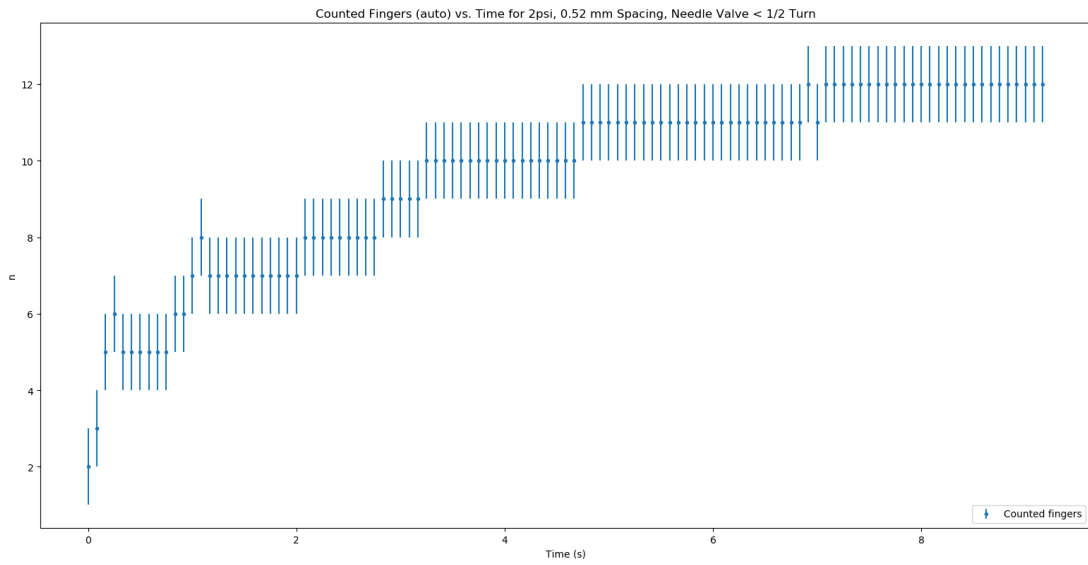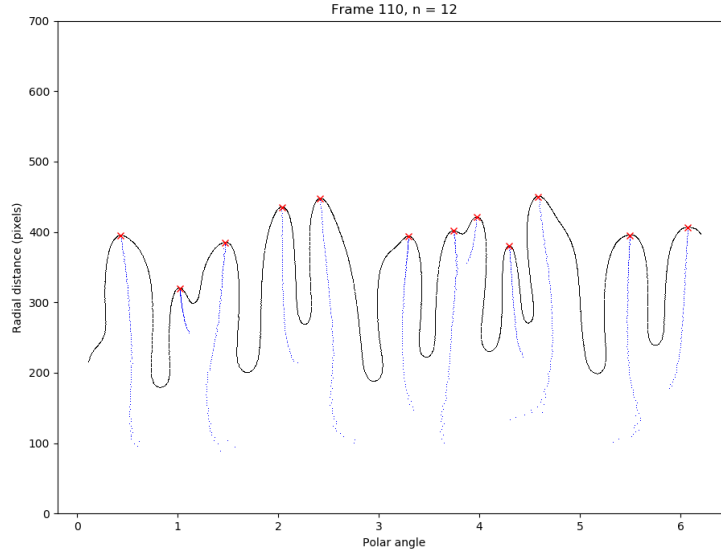

(b) In cases with few fingers, n grows continuously throughout the run.

FIG. 16: n against time throughout the entire growth of selected bubbles.

(a) Finger tip positions tracked throughout a run at 5 psi, with 1.051 mm plate spacing (also represented in Figure 16a).

(b) Finger tip positions tracked throughout a run at 2 psi with the needle valve less than 1/2 turn open, and 0.52 mm plate spacing (also represented in Figure 16b).

FIG. 17: Radial coordinate vs. polar angle for the final frame of selected runs. Finger tips present at the end of the run are marked with a red 'X'. Blue dotted lines indicate the paths of the finger tips throughout the growth of the bubble.

IV.   CONCLUSIONS

We studied fractal viscous fingering phenomena for an air bubble displacing mineral oil in a Hele-Shaw cell, in flow speed regimes specified by Reynolds number ranging between approximately 0.03 and 3.4.

In general, predictions for the growth rates of various modes of the instability giving rise to the fingering phenomenon, based on existing linear stability analysis, failed to accurately predict how many fingers would form for the regimes of Re studied. This is true of predictions

based on initial values of R/b and Ca for a given run, and those based on integrating growth rates throughout the initial growth of a bubble. The greatest discrepancy between prediction and observation occurred for the narrowest plate spacing; we suggest that a more advanced theory taking into account the wetting layer left behind on the plates as air displaces oil may have more success in these cases. Furthermore, at fixed plate spacing, theory performed worst at higher interface speeds, where the Stokes flow approximation is least valid. The predictions of linear stability theory may also have more success for an experiment that is more effectively controlled for the stochastic processes that initiate finger formation allow-

ing the instability to be caused by a perturbation more closely resembling the uniform 'noise' the theory assumes.

In the regime of nonlinear growth, we found that shadowing had a very small effect on the number of fingers present, as fingers would remain small, but seldom disappear. Tip splitting had a more significant effect, particularly in runs with a small number of broad fingers. With more fingers, tip splitting would mostly occur toward the end of bubble growth when fingers are broadest. The techniques we employed in our study may be used to examine viscous fingering phenomena at higher speeds, to track how n increases throughout a run for bubbles exhibiting more manifestly fractal behaviour.

---

[1] Y. Couder, *Perspectives in Fluid Dynamics: A Collective Introduction to Current Research*. Cambridge University Press, 2002.

[2] D. Acheson, *Elementary Fluid Dynamics*. Oxford University Press, 1990.

[3] T. Maxworthy, "Experimental study of interface instability in a Hele-Shaw cell," *Physical Review A*, vol. 39, no. 11, pp. 5863–5866, 1989.

[4] J. Miranda and M. Widom, "Radial fingering in a Hele-Shaw cell: a weakly nonlinear analysis," *Physica D: Nonlinear Phenomena*, vol. 120, no. 3, pp. 315 – 328, 1998.

[5] S. Morris, "Advanced Physics Laboratory: Fractal Viscous Fingering," 2017. [Online]. Available: https://www.physics.utoronto.ca/~phy326/fvf/

[6] P. G. Saffman and G. Taylor, "The Penetration of a Fluid into a Porous Medium or Hele-Shaw Cell Containing a More Viscous Liquid," *Proceedings of the Royal Society of London A*, vol. 245, no. 1242, pp. 312–329, 1958.

[7] E. O. Dias and J. A. Miranda, "Wavelength selection in Hele-Shaw flows: A maximum-amplitude criterion," *Phys. Rev. E*, vol. 88, p. 013016, Jul 2013.

[8] C.-W. Park and G. M. Homsy, "Two-phase displacement in Hele Shaw cells: theory," *Journal of Fluid Mechanics*, vol. 139, p. 291–308, 1984.

[9] D. A. Reinelt, "Interface conditions for two-phase displacement in Hele-Shaw cells," *Journal of Fluid Mechanics*, vol. 183, p. 219–234, 1987.

Appendix A   AUTOMATED FINGER COUNTING

A Python script entitled `count_run_FVF.py` for automated finger counting takes as its input all the binarized images from a run, after they have been *skeletonized* in `ImageJ` (modified such that black lines are only 1-2 pixels thick). It searches through a PIL image matrix for black pixels (greyscale value of 0) and records their radial coordinate value and polar angle value (using x- and y-distances from a stipulated centre point), beginning where the curve is broken due to the removal of the pipe, and travelling along the curve by finding the nearest black pixel to the most recent black pixel identified. In this case, the black pixels are indexed by the

order in which they are found; the result is a curve of r vs. this index. This curve is single valued at every point. Thus, after Savitzky-Golay smoothing is applied to the curve to prevent double-counting due to scatter, the program may treat it as a function (see Figure 18) and identify the number of fingers as the number of local maxima present. A similar method had previously been attempted, which instead searched for peaks in an r vs ϕ plot, but 'overhangs' where the fingers widen along the radial direction caused it to identify peaks where there was no tip of a finger. Using this program, a value of n could be associated with every frame in a run.

If desired, `count_run_FVF.py` also generates a plot of r vs ϕ for every frame of a given run, with a red X marking where each fingers tip is identified, and blue dotted lines tracking where finger tips were present in previous frames, as seen in Figure 17. These plots can be used to produce videos that serve as a dynamic visualization of the effects at play in fractal viscous fingering phenomena.

This algorithm is subject to some of the sources of error associated with manual finger counting, such as the gap in the boundary not captured in the image due to the inlet pipe. However, it defines a finger concretely as a point were, when moving along the boundary, the radial coordinate peaks. It does not return accurate values of n for the beginning of a run, when fingers are not yet present, but there may still be a few peaks in the radial distance due to the slightly elliptical shape, or displacement from the centre, of initial bubbles.
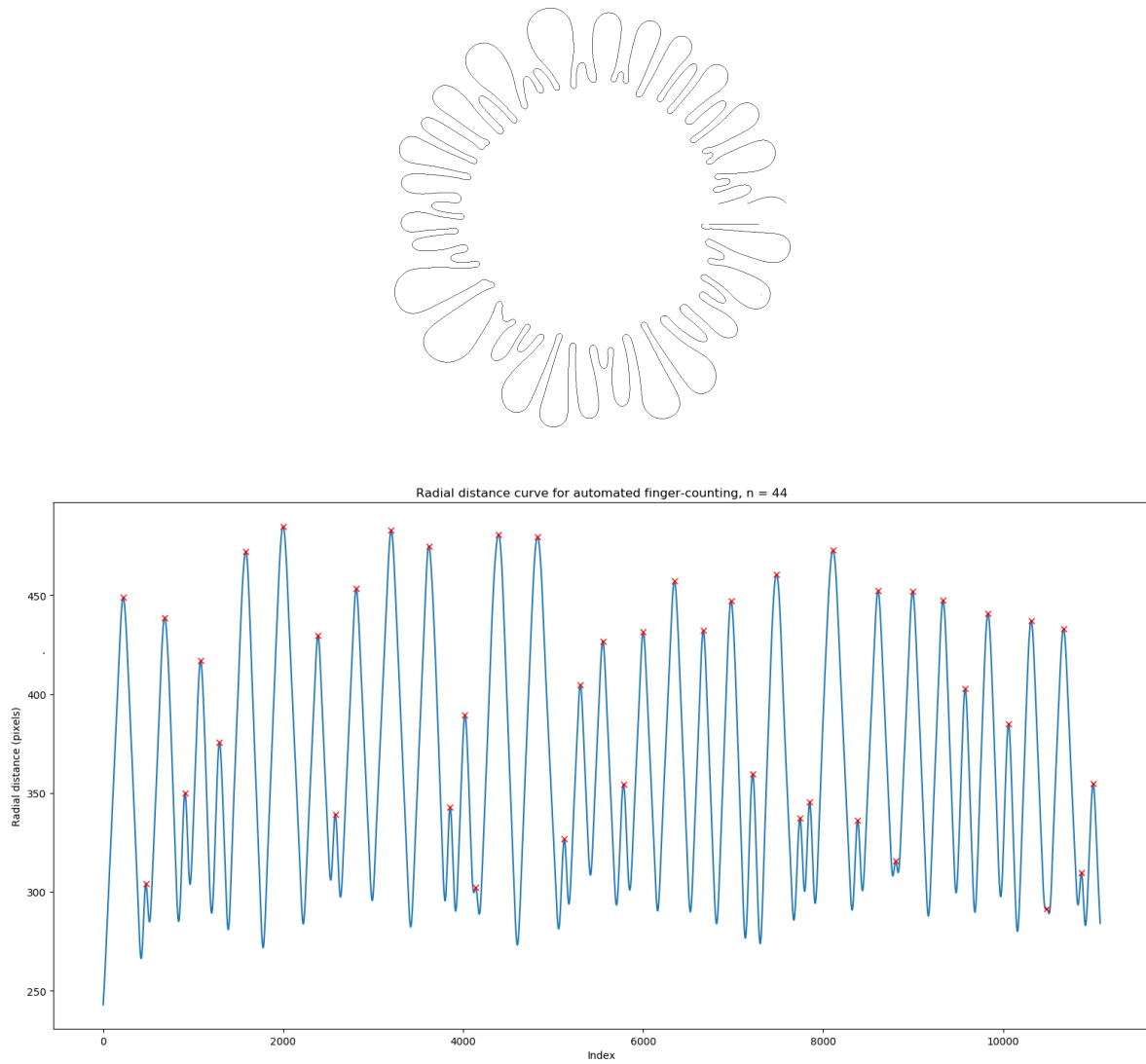
FIG. 18: A radial distance vs. 'counting index' curve for the image shown above. As a visual aid, the location of each the 44 finger tips identified by the program is marked with a red X.

Appendix B   USEFUL PYTHON SCRIPTS

A   process_FVF_images.py

Produces a set of binarized images from the set of raw images captured in a given run. May decimate the data so there are fewer binarized images than there were frames captured. Uses functions defined in kill_outliers.py to ensure that only the boundary of the bubble remains in the binarized image.

B   FVF_getradius.py

Given a set of binarized images, identifies the pixel closest to the centre of the initial bubble. Subsequently produces a .txt file of all the values of R (max, min, mean, and standard deviation) and v from throughout a run. Produces a plot of the values associated with R.

C   velocity_vs_R_FVF.py

Uses data from the .txt files produced using FVF_getradius.py to plot boundary speed, capillary number, and Reynolds number against radius throughout the initial, circular phase of a bubble's growth.

D   plot_fingers_FVF.py

Using the .txt files produced using FVF_getradius.py, calculates and saves predicted values of n for each run of the experiment, based on both integration of growth rates and initial values. Uses functions defined in sigma_bv.py. Generates a variety of plots for representing how these predictions compare with observed values.

E   finger_count_FVF.py

Counts the number of fingers present in one skeletonized, binarized image of an FVF bubble. Generates an 'unfolded' plot representing the boundary's radial distance vs polar angle, and indicates the locations of the finger tips it identifies.

F   count_run_FVF.py

See Appendix A. Applies the technique of finger_count_FVF.py to every frame in a run. Generates a plot of n against time for a single run, and a series of the 'unfolded' plots that indicate the tips of fingers. These plots can be combined to produce a video demonstrating the formation of fingers throughout a bubble's growth.

G   composite_image.py

Generates from a set of skeletonized, binarized images associated with a run a composite image of the boundary throughout the growth of a bubble.